All-water-based solution processed Ag nanofilms for highly efficient electrocatalytic reduction of CO$_2$ to CO

Sung Min Lee[1], Hyunju Lee[1], Junhyeong Kim, Sang Hyun Ahn[*], Suk Tai Chang[*]

School of Chemical Engineering and Materials Science, Chung-Ang University, 84 Heukseok-ro, Dongjak-gu, Seoul 06974, Republic of Korea

ABSTRACT

Electrochemical reduction for conversion of CO$_2$ to value-added chemicals is considered a promising method to relieve global warming. To develop a highly active and selective electrocatalyst for efficient CO$_2$ conversion, it is essential to overcome the large overpotential and to suppress the competitive hydrogen evolution reaction (HER). Herein, we report a simple and controllable fabrication method for Ag electrocatalytic films using all-water-based solution processes via a seed-mediated metal growth technique. Varying the deposition conditions allows the N/S doping ratio in Ag films with high coverage and good adhesion to be easily controlled in the range of 1.14–8.23. The doping ratio has a significant effect on the CO Faradaic efficiency (FE), as the S content modulates the binding energy of reaction intermediates, whereas the N content is effective for suppressing the HER on the Ag film surface.

1. Introduction

As a countermeasure to serious global warming, various technologies for CO$_2$ capture, utilization, and storage have been widely investigated to reduce the concentration of CO$_2$ in the atmosphere [1–4]. As a CO$_2$ utilization method, electrochemical conversion has received considerable attention for CO$_2$ removal and the production of value-added chemicals at room temperature and under ambient pressure [5–9]. This process could be made completely eco-friendly by using electricity generated from renewable energies (e.g., sunlight and wind) as the driving force for electrochemical conversion [10]. In addition, as an energy storage method, this process can complement renewable energies to address discontinuity problems [10]. Depending on the electrocatalyst, various C1 fuels (e.g., CO, CH$_4$, HCOOH, and CH$_3$OH) can be selectively obtained from electrochemical conversion of CO$_2$ [11–22]. Among them, CO production is economically feasible because it requires only two electrons and can be used as an industrial feedstock for the Fischer–Tropsch process to produce various useful chemicals [23]. However, a large overpotential for electrochemical CO$_2$ conversion is inevitable because CO$_2$ is very stable at room temperature. Furthermore, as the hydrogen evolution reaction (HER) occurs competitively in aqueous electrolytes, high selectivity for desired product is required. Thus, the development of efficient electrocatalysts remains a great challenge.

Various Ag-based electrocatalysts have been investigated for efficient CO production owing to their reasonable activity and moderate cost [11,12,14]. For example, morphological control of pure Ag has been studied using engineered nanostructures such as nanoporous Ag [11], Ag corals [24], Ag inverse opal structures [15], Ag dendrites [25], Ag nanosheets [26], Ag foams [27], and triangular Ag nanoplates [28]. The CO Faradaic efficiency (FE) is enhanced by certain high-index facets [16] or by changes in the local pH [29] at the catalyst surface. Furthermore, the roughened surface of Ag electrocatalysts provides a large electrochemical surface area (ECSA) to increase the CO production rate. Using controlled morphologies, Ag-based alloys [12,30,31] and oxide-derived Ag [32] have also been investigated to modify the Ag electronic structure, thus enhancing the CO FE and production rate. Recently, density functional theory (DFT) calculations predicted that a Ag-based electrocatalyst doped with S would decrease the overpotential for electrochemical conversion of CO$_2$ to CO [33]. This prediction has been experimentally confirmed using a 5 nm Ag nanoparticle (NP) electrocatalyst synthesized using an anchoring agent (cysteamine) [34]. Further enhancement of the catalytic performance has been realized by post-treatments such as amine treatment and thiol treatment of cysteamine-anchored Ag NP/C (CA Ag/C) [35]. Although the optimal binding energy of ˙COOH intermediates is obtained with thiol-treated CA Ag/C, the highest CO FE is achieved with amine-treated CA Ag/C because the competitive HER is efficiently suppressed by the decreased

---

H binding energy on the surface of amine-treated CA Ag/C. However, the correlation between the catalytic performance and the N/S doping ratio in Ag-based electrocatalysts has not yet been reported.

Electrocatalytic Ag-based thin films can be simply prepared by surface modification of Ag foil or Ag electrodeposition on a substrate [14,24,25,27,36–39]. As a Ag foil has a small ECSA, morphological modification (e.g., chemical etching) is essential, but a large amount of Ag is wasted in such processes. Lower Ag utilization is inevitable because most of the Ag foil serves as a substrate. Thus, there are issues associate with the practical use of surface-modified Ag foils [14,24,36–38]. As an alternative, electrodeposition has been considered a simple and effective method to prepare electrocatalytic Ag-based films. Varying the deposition conditions enables easy control of the morphology and composition. Furthermore, certain facets can be highly populated by adding various additives. However, the large amount of waste solution generated during electrodeposition is a cause of environmental concern and large-area processes produce nonuniform Ag films owing to the potential difference along the working electrode [25,27,39]. Therefore, effective and efficient fabrication processes should be developed for Ag-based thin film electrocatalysts.

In this study, we report a cost-effective fabrication process for an electrocatalytic Ag film for electrochemical CO_2 conversion. The Ag film was directly grown on an aminosilane-deposited substrate by a seed-mediated metal growth technique; thus, the Ag film was bound on the substrate via amine groups, which have high affinity for Ag. The adhesion strength of the Ag film on the substrate was verified by a peel-off test based on the ASTM D3359 standard test method, and negligible damage of only 0.01% was observed after the peel-off test. The N/S doping ratio was controlled by adjusting the density of the aminosilane layer and thiol-treated seed particles. Based on this strategy, we investigated catalytic activity of Ag films with N/S doping ratios in the range of 1.14–8.23. The catalytic activity of the Ag electrocatalyst film was significantly enhanced with N/S doping ratios between 1.75 and 2.89, especially in the low overpotential region. Within this range of N/S doping ratios, an excellent CO FE of 75.7% was obtained at −0.3 V_{RHE}.

2. Experimental

2.1. Preparation of self-assembled monolayers (SAMs) on substrates

As substrates, glass slides (76 mm × 26 mm, Paul Marienfeld GmbH & Co. KG) and silicon wafers (300 nm wet oxidation, Namkang Hi-Tech Co., Ltd.) were cleaned using piranha solution. To prepare a SAM, the precleaned substrates were immersed in a mixture of deionized water and aminosilane ((3-aminopropyl)triethoxysilane (APTES, 440140, Sigma Aldrich) or N^1-(3-trimethoxysilylpropyl)diethylenetriamine (DETA, 413348, Sigma Aldrich)) for 1 h. The detailed conditions are summarized in Tables 1 and 2. The SAM-coated substrates were washed with deionized water and dried under a stream of nitrogen gas. Then, the substrates were annealed on a hotplate at 120 °C for 30 min to complete the silanization reaction. After the annealing process, unreacted residues were removed by sonication (5800, Branson) in a deionized water bath for 30 min.

2.2. Fabrication of Ag films on SAM surfaces

First, a Au NP solution was prepared. Deionized water (400 mL) was heated on a hotplate at 130 °C with stirring at 600 rpm. When the water began to boil, 138 μL of 30 wt.% $HAuCl_4$ solution (484385, Sigma Aldrich) was added. After mixing well, 40 mL of sodium citrate solution (62 mM, S4641, Sigma Aldrich) was added, and the color of the solution changed from yellow to colorless, black, purple, red, and wine-red. The wine-red solution was heated with stirring for a further 30 min and then cooled with stirring to room temperature. The solution was highly concentrated by centrifugation (Supra 22k, Hanil Science Medical) with

Table 1
Coating conditions for Ag electrocatalyst films with various coverages.

Sample	Au NP coating			Ag enhancement				Annealing	Ag coverage/%
	Solution concentration/wt%	Coating time/ min	Number of coating/#	Solution concentration	Solution volume/μL cm^{-2}	Enhancement time/min	Number of coatings/#		
Ag52.5	0.04	10	1	50% DI water 50% enhancer[a]	25	5	1	300 °C for 20 min	52.5
Ag68.0	0.04	10	1	40% DI water 60% enhancer	25	5	1		68.0
Ag87.8	0.04	10	1	100% enhancer	25	5	1		87.8
Ag99.2	0.04	10	1	100% enhancer	25	5	2		99.2

[a] Enhancer: 1:1 mixture of Ag enhancer solution A and B.

Table 2
Coating conditions for Ag electrocatalyst films with various N/S ratios.

Sample	SAM layer	Au NP coating				Ag enhancement				Surface composition (XPS)				
		Au NP concentration/wt%	MPA[a]	Deposition method	Number of coating/#	Enhancer concentration/%	Solution volume/μL cm^{-2}	Enhancement time/min	Number of coatings/#	Au/%	Ag/%	N/%	S/%	N/S ratio
Ag1.14	0.1% APTES	0.3	–	MDD[b]	1	100	25	5	1	2.40	51.38	3.66	3.21	1.14
Ag1.33	0.1% APTES	0.3	Added	MDD	2	100	25	5	1	2.60	58.32	2.74	2.06	1.33
Ag1.75	0.1% APTES	0.3	Added	MDD	1	100	25	5	1	1.41	45.31	3.23	1.85	1.75
Ag2.89	0.1% APTES	0.04	Added	MCDC[c]	1	100	25	5	2	1.10	56.28	2.51	0.87	2.89
Ag4.63	5% DETA	0.04	–	MCDC	1	100	25	5	2	0.63	55.20	3.38	0.73	4.63
Ag8.23	0.1% APTES	0.04	–	MCDC	1	100	25	5	2	0.68	58.27	2.55	0.31	8.23

[a] MPA: mercaptopropionic acid.
[b] MDD: meniscus-dragging deposition.
[c] MCDC: micro-contact dip coating.

a filter (Amicon Ultra-15 100 K, Merck) at 2000 *g* for 20 min. Then, the concentrated solution was quantified by UV–vis spectroscopy (V-670, Jasco) and diluted with the filtered solution to obtain the desired concentration.

Au NP deposition on the SAM surface was achieved by microcontact dip coating (MCDC) and meniscus-dragging deposition (MDD) [40]. Schematic illustrations of the MCDC and MDD processes are shown in Figs. 1 and S1, respectively. In the MCDC method, the Au NP solution was injected between the SAM-coated substrate and an air-plasma-treated glass slide (cover plate) separated by a 100 μm spacer. The deposition was allowed to proceed for 10 min. The substrate was then separated from the cover plate in deionized water and washed with deionized water and dried under a gently stream of nitrogen gas. The MDD method allowed deposition of a higher density of Au NPs on the SAM [41]. An air-plasma-treated glass slide as a deposition plate was placed on the SAM-coated substrate at an angle of 37°. A Au NP solution (0.3 wt.%, 42 μL) was injected at the edge between the deposition plate and the SAM-coated substrate. The deposition plate was moved 3.5 cm linearly 10 times in a back-and-forth motion by a motorized stage (AL1-1515-3S, Micro Motion Technology) at a constant speed of 10 mm s^{-1}. Then, the Au-NP-deposited substrate was dried on an 80 °C hotplate. After Au NP deposition, a mixture of Ag enhancer solution A (S5020, Sigma Aldrich) and B (S5145, Sigma Aldrich) was injected between the Au-NP-deposited substrate and an air-plasma-treated glass slide (cover plate) separated by a spacer with varying thicknesses (150 and 250 μm). The Ag enhancement process was allowed to proceed for

5 min. Then, the substrate was separated from the cover plate in deionized water, washed with deionized water, and dried under a gentle stream of nitrogen gas. The obtained film was annealed at 300 °C at least 5 min.

2.3. Treatment with 3-mercaptopropionic acid (MPA)

Several Ag films were prepared by adding MPA (M5801, Sigma Aldrich) to the Au NP solution. For the MCDC method, 0.5 mM MPA (400 μL) was directly added to a 0.04 wt.% Au NP solution, whereas 2.5% of a 8 mM MPA solution was added to a 0.01 wt.% Au NP solution for the MDD method. Then the solutions were kept in a refrigerator for 12 h. The MPA-added 0.01 wt.% Au NP solution was highly concentrated by centrifugation (Supra 22k, Hanil Science Medical) with a filter (Amicon Ultra-15 100 K, Merck) at 2000 *g* for 20 min. Then, the concentrated Au NP solutions were quantified by UV–vis-NIR spectroscopy (V-670, Jasco) and diluted with the filtered solution to obtain a concentration of 0.3 wt.% for MDD.

2.4. Characterization

The concentration of Au NPs was calculated from the amount of added Au, assuming that most Au reacted successfully. The morphologies of the fabricated films were imaged using optical microscopy (Olympus BX-51), field emission scanning electron microscopy (FE-SEM; Sigma, Carl Zeiss), and an IR thermal camera (M8, Wuhan Guide
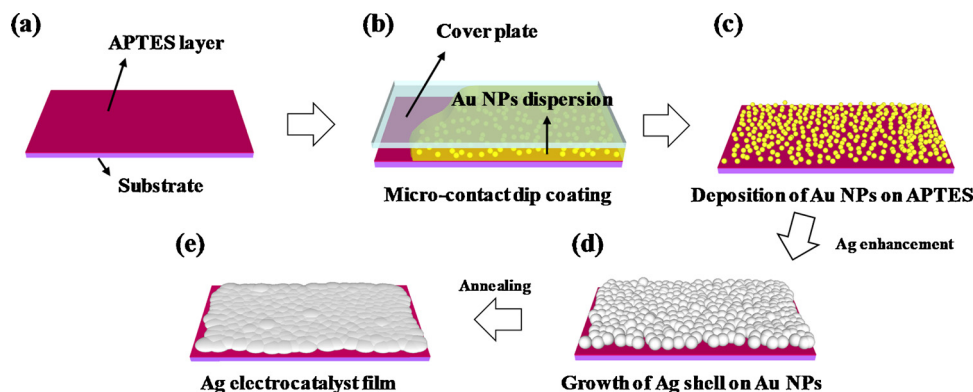

Fig. 1. Schematic illustration of the MCDC method for Ag film fabrication. (a) APTES deposition on a glass slide or Si wafer. (b) MCDC of the Au NP solution. (c) Deposition of Au NPs on the APTES layer. (d) Ag shell growth on the Au NPs. (e) Ag film after annealing.
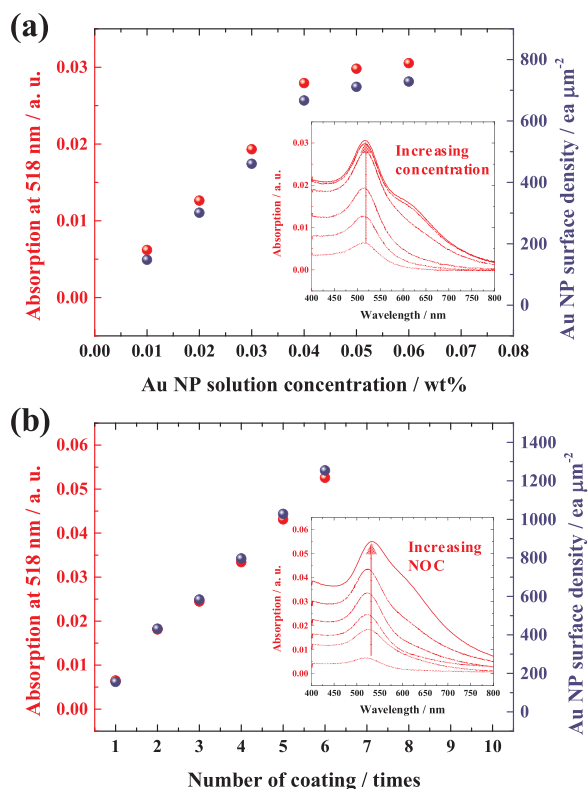
Fig. 2. Absorbance and surface density of Au NPs deposited on a glass slide substrate depending on (a) the Au NP solution concentration and (b) the number of coating steps (insets: corresponding UV–vis absorption spectra).

Infrared Co., Ltd.). The sheet resistance was measured using a Keithley 2602A sourcemeter with a four-point probe system (MSA001, MS Tech). The optical transmittance was measured by UV–vis-NIR spectroscopy (V-670, Jasco). The electronic structures were determined by X-ray photoelectron spectroscopy (XPS; K-Alpha+, Thermo Fisher Scientific). The crystal structures were analyzed by X-ray diffraction (XRD; New D8-Advance, Bruker).

2.5. Electrochemical CO_2 conversion

Electrochemical CO_2 conversion was performed in a H-type cell (Pine Research Instrumentation). Each cathode and anode compartment had a volume of 25 mL and was separated by a Nafion 212 membrane (thickness: 50 μm, Dupont Co.). In the cathode compartment, the prepared Ag catalyst film sealed in a lab-made holder with an exposed area of 0.50 cm^2 was employed as the working electrode, and a saturated calomel electrode was used as the reference electrode. In the anode compartment, commercial Pt gauze was employed as the counter electrode. The electrolyte in both the cathode and anode compartments was a 0.5 M $KHCO_3$ (99.5%, Daejung) solution (pH 7.3). Before electrochemical CO_2 conversion, the catholyte and anolyte were purged by bubbling CO_2 and N_2 gas, respectively, for 30 min. To maintain CO_2 saturation in the catholyte, CO_2 gas was continuously injected at a rate of 10 sccm during the experiment. Several potentials were applied for 30 min using chronoamperometry, controlled by a potentiostat (DY2311, Digi-Ivy). CO and H_2 produced in the cathode compartment were analyzed by gas chromatography (Agilent 7890A) equipped with a flame ionization detector and a thermal conductivity detector. Based on the amount of electrical charge and the concentration of products, the FE was calculated. As a reference, electrochemical CO_2 conversion was also conducted on commercial Ag foil (thickness: 280 μm, 41451, Alfa Aesar).

3. Results and discussion

3.1. Fabrication and characterization of electrocatalytic Ag films

The details of the fabrication processes for the electrocatalytic Ag films are illustrated in Fig. 1. Cost-effective fabrication was achieved by combing colloidal Au NP deposition with subsequent Ag enhancement. As a SAM, APTES was chosen to give amine functional groups on the substrate surface (Fig. 1a). After formation of an APTES layer on the substrate, the MCDC method was introduced to minimize solution consumption during colloidal Au NP deposition on the surface of the APTES layer (Fig. 1b). Spontaneous spreading of the Au NP solution between the APTES layer and the cover plate was observed owing to the enhanced capillary force achieved by the high surface energy of the air-plasma-treated cover plate. As a result, uniform deposition of Au NPs was obtained (Fig. 1c), confirming good electrostatic adhesion between the Au NPs and the amino groups [40,42]. Similarly, through the MCDC method, uniform growth of a Ag shell was also achieved by Ag enhancement on the surface of the pre-deposited Au NPs (Fig. 1d) [43,44]. These approaches allowed solution consumption to be greatly reduced to the microliter scale for deposition over an area of a square centimeter, whereas conventional dip coating requires solutions on the milliliter scale to fill the deposition bath. Subsequently, the sample was annealed on a hotplate at 300 °C for at least 5 min to increase the conductivity of the Ag film (Fig. 1e). Then, XRD pattern of the Ag thin film was investigated as shown in Fig. S2. The three distinct diffraction peaks were observed at 2θ = 38.2°, 44.5°, and 64.6°, which are well matched with standard crystal planes of face-centered cubic Ag structure [JCPDS card no. 4-0783] [45,46].

To confirm the controllability of the MCDC method for reliable Ag film fabrication, UV–vis spectroscopy was used to investigate various Au NP deposition parameters. Fig. S3a shows the importance of the APTES layer for electrostatic adhesion of Au NPs from a 0.01 wt.% Au NP solution. Without the APTES layer, the absence of an absorption peak at 518 nm (inset, Fig. S3a) indicates that no Au NPs were adhered to the substrate, regardless of the dipping time in the Au NP solution bath, likely owing to electrostatic repulsion between the Au NPs and the negatively charged hydroxyl groups formed on the glass substrate after piranha cleaning. In contrast, with the APTES layer, an absorption peak was observed at 518 nm after a dipping time of 15 min, and the absorbance gradually increased as the dipping time increased because the positively charged amine groups in the APTES layer provided sufficient electrostatic attraction for Au NP deposition. The Au NP surface density was analyzed quantitatively by manually counting the particles observed in FE-SEM images and plotted as a function of the obtained absorbance, as shown in Fig. S3b. For Au NP surface densities lower than 1600 ea μm^{-2}, a linear relationship was observed. However, further increasing the coating time (> 60 min) resulted in deviation from the linear relationship owing to severe aggregation of the deposited Au NPs, which inhibited precise determination of the number of deposited Au NPs. Fig. 2a shows Au NP surface density obtained by MCDC as a function of the concentration of the Au NP solution (0.01–0.06 wt.%) at a constant coating time of 10 min. For concentrations lower than 0.04 wt.%, the Au NP surface density increased linearly, but saturation was observed with further increases of the concentration of the Au NP solution. Based on these results, a strategy for precise control of the Au NP surface density was chosen, namely, using MCDC and a 0.01 wt.% Au NP solution, the number of coating steps, each with a coating time of 10 min, was varied, as shown in Fig. 2b. With an increase of the number of coating steps from 1 to 6, the Au NP surface density linearly increased from 155 to 1254 ea μm^{-2}, corresponding to the increase in absorbance in the UV–vis spectra. The corresponding FE-SEM images are shown in Fig. S4.

Ag enhancement was performed on the deposited Au NPs by MCDC using commercial Ag enhancer solutions (15 μL cm^{-2}) for 5 min. Fig. 3a shows the UV–vis spectra of Ag films with various Au NP surface
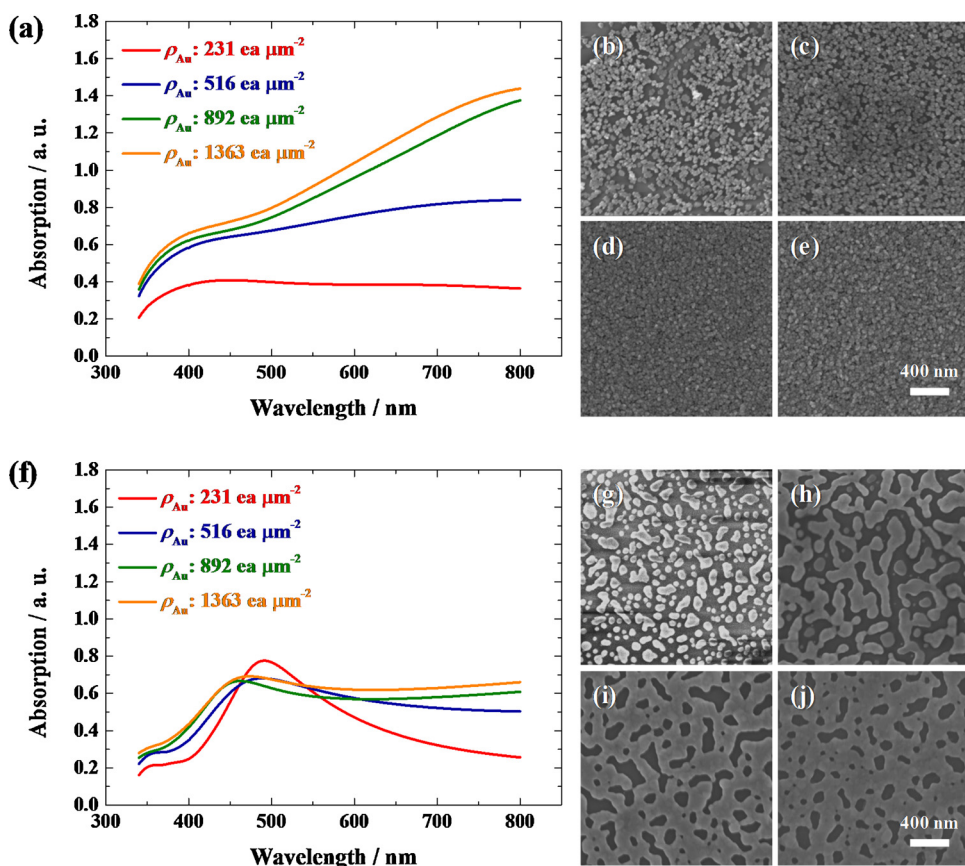
Fig. 3. UV–vis absorption spectra of Ag films with various Au NP surface densities (a) before and (f) after annealing. Corresponding FE-SEM images of Ag films prepared with Au NP surface densities of (b) 231 ea μm^{-2}, (c) 516 ea μm^{-2}, (d) 892 ea μm^{-2}, (e) 1363 ea μm^{-2}, (g) 231 ea μm^{-2}, (h) 516 ea μm^{-2}, (i) 892 ea μm^{-2}, and (j) 1363 ea μm^{-2}.

densities after Ag enhancement. The absorbance increased with an increase of the Au NP surface density, especially at wavelengths above 600 nm, indicating that Ag enhancement was promoted at higher Au NP surface densities. The increased absorbance in the wavelength range of 400–600 nm corresponds to the characteristic peak of Ag-enhanced Au NPs [47]. The corresponding FE-SEM images (Fig. 3b–e) demonstrate that individual enhanced Ag particles had sizes of approximately 50 nm and that the density of Ag particles increased with an increase of the Au NP surface density. As shown in Fig. 3f, after annealing at 300 °C for 5 min, obvious absorption peaks appear in the wavelength range of 400–500 nm and the absorbance at wavelengths longer than 600 nm is significantly decreased. The changes in the absorption spectra after annealing can be explained by the corresponding FE-SEM images (Fig. 3g–j). At a Au NP surface density of 231 ea μm^{-2}, the enhanced Ag particles melted and agglomerated to form nanosized islands after annealing (Fig. 3g). Therefore, owing to the size-dependent light absorption characteristics caused by the larger domain size, the absorbance at longer wavelengths decreased [48]. As the Au NP surface density increased, the nanosized islands grew gradually, and then formed connections with each other (Fig. 3h–j), resulting in an increase of surface coverage. In addition, the sheet resistance of the Ag film was drastically decreased after annealing (Fig. S5).

The morphologies of the Ag films could also be controlled by varying the amount of Ag enhancement solution and adjusting the spacer thickness between the cover plate and the APTES-coated substrate (Fig. 1b). Fig. S6a–d shows the morphologies of enhanced Ag particles obtained using a solution volume of 25 $\mu L\ cm^{-2}$ depending on the Au NP surface density. The sizes of individual Ag particles were approximately 70 nm, which is 40% larger than those obtained using a 15 $\mu L\ cm^{-2}$ solution (Fig. 3b–e). In addition, the density of Ag particles increased as the Au NP surface density increased. After annealing (Fig. S6e–h), larger nanosized islands were observed at the lowest Au NP surface density of 231 ea μm^{-2}. Ag coverage was also increased by

increasing the Au NP surface density, with a maximum coverage of 90% obtained at the highest Au NP surface density of 1363 ea μm^{-2}.

To confirm stable adhesion of the Ag film to the substrate, two types of adhesion strength tests were conducted to verify the resistance against exfoliation and delamination based on standard test method D3359 using filament-enhanced adhesive tape, which has an adhesion strength of 7.1 N cm^{-1} to steel. Fig. 4a shows a schematic illustration of the adhesion test. First, the exfoliation ratio was calculated by comparing absorbance of the Ag film before and after the peeling-off test. An uncut bare Ag film was used for the test. Fig. 4b shows change in absorbance at 550 nm after the peeling-off test as a function of number of peeling-off tests performed (0–3). A negligible decrease in absorbance was observed, indicating that the Ag film had strong exfoliation resistance. Notably, 99.2% of the film remained after the peeling-off test, and even after three peeling-off tests, 98% of the Ag film still remained.

To investigate the delamination resistance, the Ag film was manually cut into 2 mm intervals to form 100 test cells, as shown in Fig. 4c–f. The delamination ratio of test cells was calculated by comparing the gray value of the obtained images before and after the adhesion test. For precise calculations, high-resolution images with more than 2000 × 2000 pixels were obtained by optical microscopy at the same position for the 100 test cells before and after the peeling-off test. Fig. 4c and d shows optical images of the Ag film before and after the peeling-off test. Only negligible delamination was observed (0.01%), which may have been caused by remaining residues in the cut areas. Fig. 4e and f shows maps of the ratio of remaining area in the 100 test cells after the peeling-off test. The average delamination ratio was calculated to be only 0.0426% over the 100 test cells, and the most delaminated cell had a delamination ratio of only 0.17%. Based on D3359 classification, the Ag film can be classified as B5 grade, which is the strongest adhesion grade. The strong adhesion strength of the Ag film results from the covalent bonds between the APTES layer and Ag.
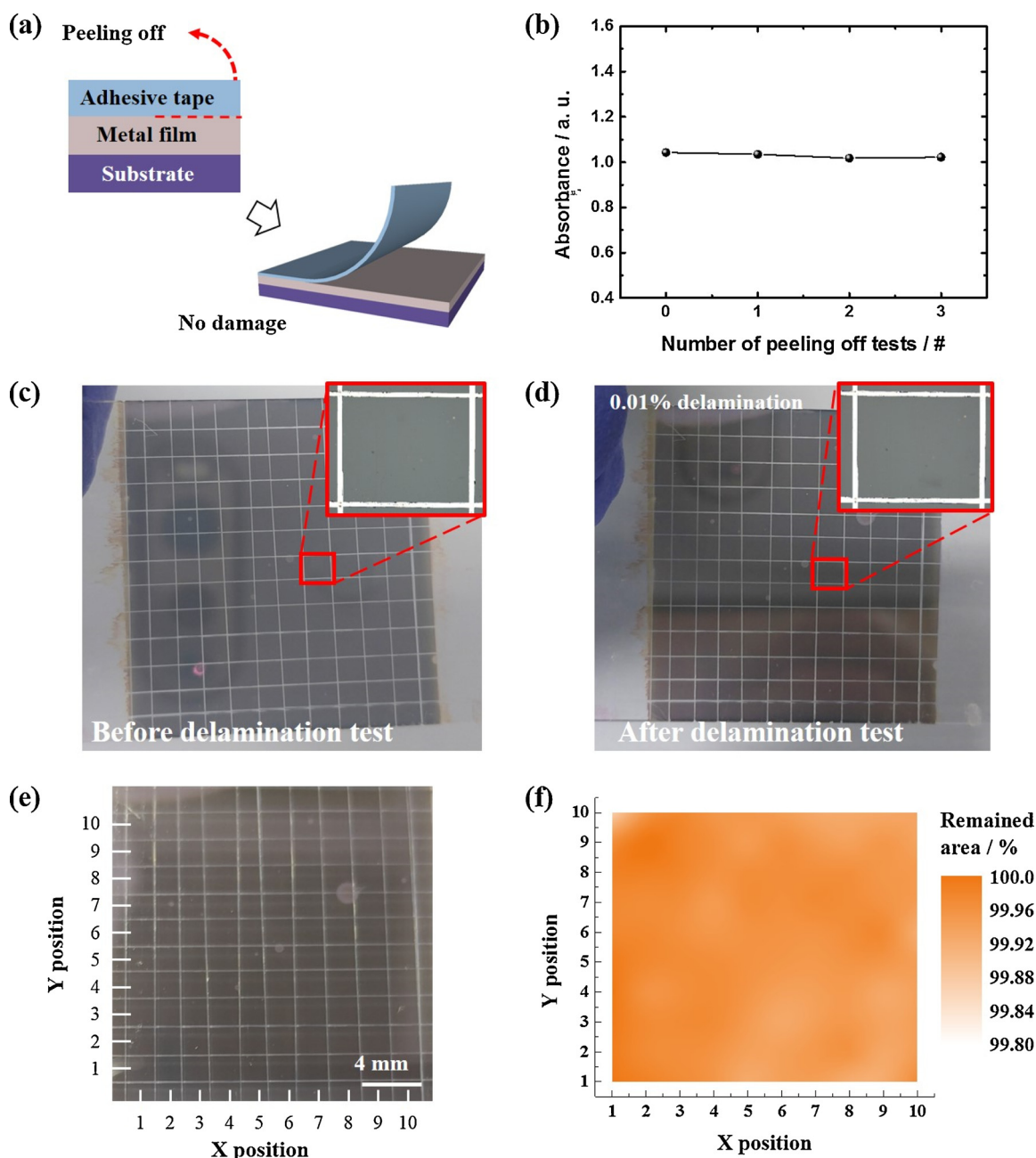
Fig. 4. Adhesion characterization by the D3359 method. (a) Schematic illustration of the D3359 method. (b) Absorbance at 550 nm depending on number of peeling-off tests. Optical microscope image of the Ag film (c) before and (d) after the delamination test. Mapping analysis: (e) analytic area (10 × 10) and (f) remaining area ratio.

APTES, which is strongly bonded to the substrate through siloxane bonds, has amine functional groups on the opposite end of its molecular chain that can covalently bind Ag via π-back-bonding [49]. Thus, the Ag film is strongly bonded to the substrate, enabling stable operation as an electrocatalyst without delamination.

3.2. Electrochemical reduction of CO_2 on Ag films

Based on the results in Section 3.1, various Ag films with different coverages were prepared to examine their catalytic activity for electrochemical CO_2 reduction. The Ag film coverage was controlled between 52.5% and 99.2%, as shown in Fig. 5a–d, by varying Au NP coating and Ag enhancement parameters such as the solution concentration, and number of coating steps, as summarized in Table 1. The Ag film samples were denoted as Ag# (#: Ag coverage in %). Fig. 5e

depicts the CO FE at -0.7 V_{RHE} after 30 min. As the Ag coverage increased, the CO FE gradually increased from 23.3% to 79.6%, likely indicating that the stepped sites in the uncovered area were less active. In addition, the stability of the Ag film with 99.2% coverage was confirmed at the potential of -0.7 V_{RHE} (Fig. S7).

To increase the catalytic activity of the Ag film, the functional groups under the Ag film were varied by using different SAMs. The Au NP coating and Ag enhancement parameters were controlled to maintain high Ag film coverage of more than 87% (Fig. S8), thus eliminating the effect of coverage on the catalytic activity. As the fabricated Ag films were thin (< 100 nm), the electronic structure at the surface of the Ag film might be affected by the N and S contents of the functional groups in the SAMs. Thus, 6 Ag films were prepared according to conditions summarized in Table 2. The samples were denoted Ag# (#: N/S ratio). According to the surface composition determined by XPS
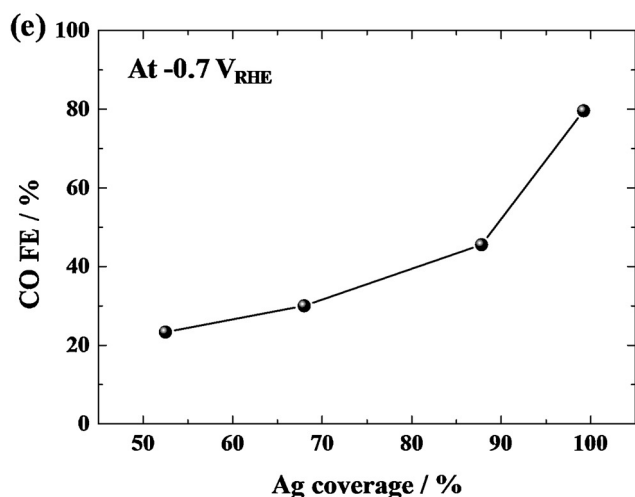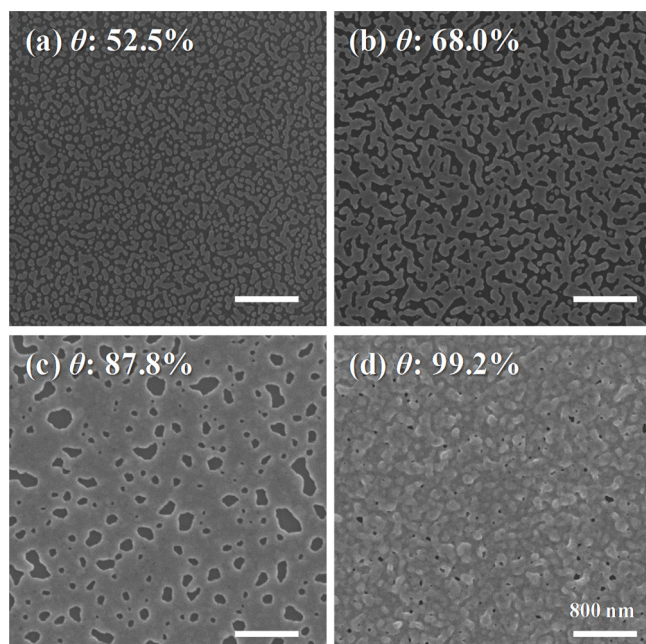
Fig. 6. Ag 3d XPS spectra of a commercial Ag foil and fabricated Ag films with different N/S ratios.

Fig. 5. FE-SEM images of Ag films with coverages of (a) 52.5%, (b) 68.0%, (c) 87.8%, and (d) 99.2%. (e) CO FE at -0.7 V_{RHE} as a function of Ag coverage.

analysis, the main component was Ag (45.3%–58.3%), while small amounts of Au, N, and S were detected from the SAM and the Au NPs. The S components may originate from the Ag enhancer solution and thiol groups in MPA-treated Au NPs. In addition, the surface composition could be affected by the thickness of the Ag film owing to the penetration depth of XPS analysis. Fig. 6 depicts the Ag 3d spectra of a commercial Ag foil and the prepared Ag films. Although there is no consistent tendency in the binding energy shift depending on the N/S ratio, all of the Ag films exhibited an obvious shift to higher binding energies relative to the Ag foil case. The binding energy of the Ag $3d_{5/2}$ peak for Ag foil was 368.18 eV, whereas those for the prepared Ag films were in a range of 368.39–368.85 eV. This shift indicates that electron transfer occurs from the Ag film to underlying N and S in the functional groups owing to differences in electronegativity (Ag: 1.9, N: 3.0, and S: 2.5). Thus, it can be said that the electronic structure of the Ag films was partially oxidized compared with pure Ag.

Electrochemical CO_2 reduction was conducted on the prepared Ag# films. The calculated CO FE values as a function of applied potential are shown in Fig. 7a. At -0.3 V_{RHE}, the highest CO FE was obtained with the Ag1.75 film (N/S ratio = 1.75). Although a small overpotential was applied (thermodynamic reduction potential for CO_2 to CO: -0.11
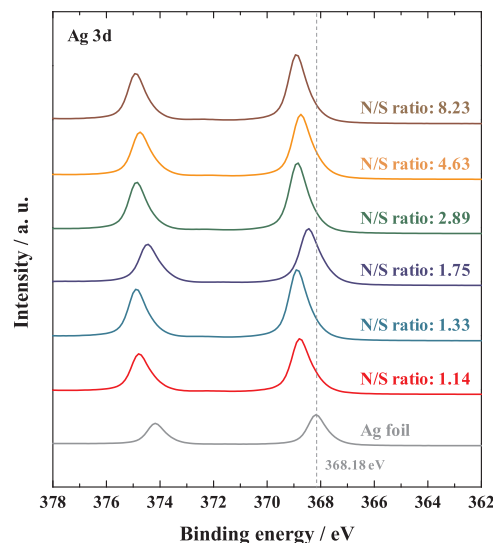
V_{RHE}), the Ag1.75 film demonstrated a high CO FE of 75.7%. When the N/S ratio was increased to 2.89 or decreased to 1.14, the CO FE decreased to 60.0% and 43.9%, respectively. Further increasing the N/S ratio to 4.63 and 8.23 resulted in a significant decrease of the CO FE to 33%. When the applied potential was negatively shifted, the CO FE for the Ag1.75 film fluctuated slightly, but maintained a high value, whereas the CO FE for the Ag1.14 film with the smallest N/S ratio remained low. However, for the high N/S ratios in the range of 2.89–8.23, significant increases in the CO FE were observed.

In the general mechanism proposed for electrochemical reduction of CO_2 to CO [50], the first step involves adsorption of a CO_2^- intermediate on the catalyst surface following transfer of one electron from dissolved CO_2. Then, the adsorbed intermediate reacts with two H^+ in the aqueous electrolyte using one more electron to produce CO and H_2O. As the first step is typically accepted as the rate-determining step [50], many studies have focused on increasing the affinity of the catalyst toward the CO_2^- intermediate [50]. One strategy is to enhance the S content of the Ag NP catalyst [34]. The enhanced catalytic performance of thiol-treated Ag/C was explained by its suitable $\Delta G_{B,COOH}$ value, which is close to the optimal value predicted by DFT. In our results, at an applied potential of -0.3 V_{RHE}, the Ag films with lower N/S ratios (≤ 2.89, i.e., relatively high S contents) demonstrated higher CO FE values than those with higher N/S ratios (≥ 4.63). The adsorption of the CO_2^- intermediate is thought to be optimized on the surface of the Ag1.75 film. As reported previously, the $\Delta G_{B,COOH}$ value of amine-treated Ag/C is less optimal than that of thiol-treated Ag/C, but its $\Delta G_{B,H}$ value is also less optimal, indicating that the competitive HER can be suppressed by increasing the N content. Based on these findings, the lower CO FE of the Ag1.14 film at -0.7 V_{RHE} compared with those of the other films can be explained by its relatively low N content. The increase of the CO FE values of the Ag films with N/S ratios of 2.89–8.23 on negatively shifting the applied potential from -0.3 to -0.7 V_{RHE} can be also explained by the higher N contents of these films, which suppress the HER. Fig. 7b shows the CO FE values as a function of the N/S ratio. At lower N/S ratios (< 1.5), the CO FE fluctuated in the range of 30%–60% owing to effects of the similar contents of N and S on the $\Delta G_{B,COOH}$ values. At higher N/S ratios (> 4.0), the N content has an obvious effect on the CO FE. At intermediate N/S ratios, higher CO FE values were obtained owing to complementary effects, as the S content optimizes CO_2^- intermediate adsorption whereas the N content suppresses the HER. Similar variations in the Ag $3d_{5/2}$ binding energy with the N/S ratio were observed (dashed line). In addition, based on the similar morphology (Fig. S8),
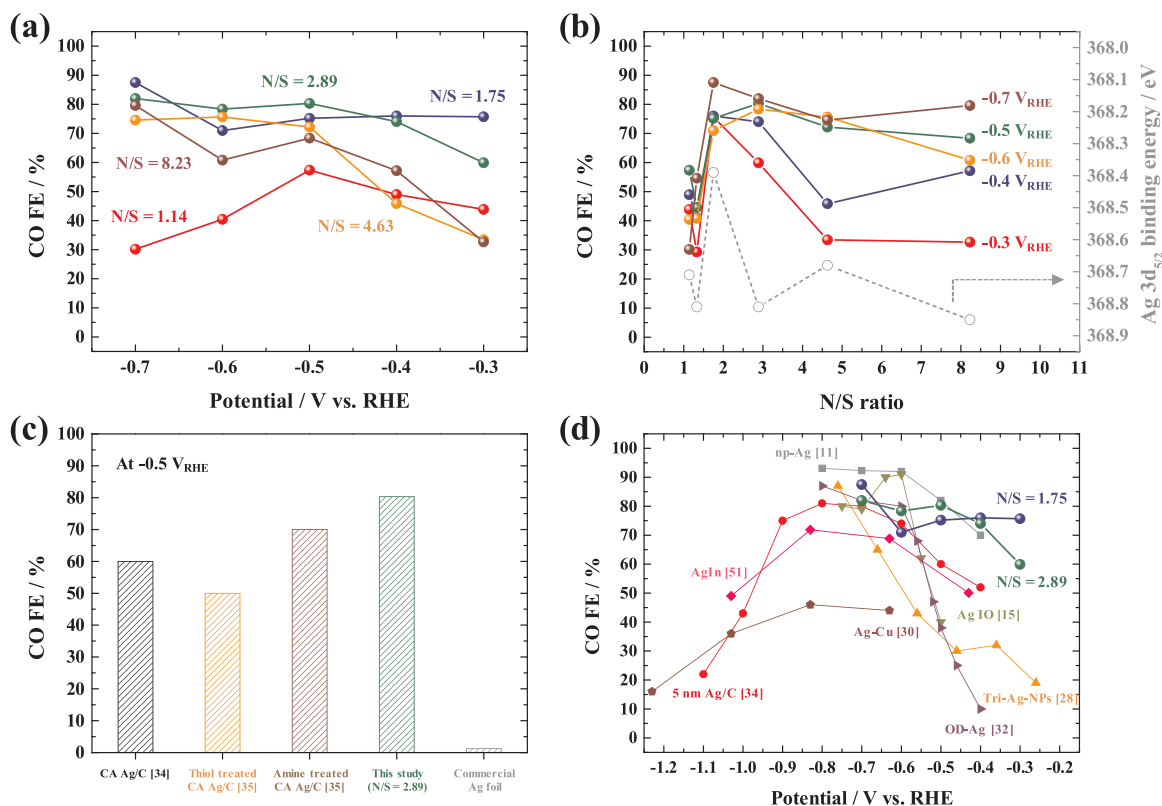
Fig. 7. (a) CO FE of Ag films depending on applied potential. (b) CO FE and Ag $3d_{5/2}$ binding energy of Ag films as a function of N/S ratio. (c) Comparison of CO FE for the Ag2.89 film with those for Ag/C [34] with thiol [35] and amine [35] treatments, and commercial Ag foil. (d) Comparison of CO FE for state-of-the-art Ag-based catalysts [11,15,28,30,32,34,51].

the CO partial current density (PCD) for the prepared Ag# films also showed significant relationship with the N/S ratio (Fig. S9), well-matched to that for CO FE. As shown in Fig. 7c, compositional control enabled the Ag2.89 film to achieve higher CO FE value than thiol-treated and amine-treated Ag/C [35]. The CO FE of 80.3% for Ag2.89 film was much higher than that of 1.3% for the commercial Ag foil, indicating the positive effect of N and S doping on CO selectivity. Furthermore, as demonstrated in Fig. 7d, Table S1, and Fig. S10, the obtained CO FE and PCD values were comparable to or higher than those of state-of-the-art Ag-based catalysts obtained by morphological control (nanoporous Ag [11], Ag inverse opal [15], Tri-Ag-NPs [28], and 5 nm Ag/C [34]) and compositional control (Ag-Cu [30], oxide-derived Ag [32], and AgIn [51]). It should be noted that the Ag films prepared in this study showed remarkably advantages in the low overpotential region, because the S content modulated the binding energy of reaction intermediates, whereas the N content suppressed the HER. During the stability test at -0.5 V_{RHE} for 10 h, the CO FE was gradually decreased without significant change in sheet resistance and morphology (Fig. S11). The XPS analysis after the test revealed the significant changes in surface composition of Ag film, which might be responsible for degradation of catalytic activity (Fig. S12).

4. Conclusion

In summary, all-water-based solution processes were developed to fabricate highly active Ag electrocatalytic films by combining colloidal Au NP deposition and subsequent Ag enhancement on APTES-deposited substrates. Based on this strategy, material consumption was minimized without emission of pollutants, providing a cost-effective fabrication method for Ag electrocatalytic films. Moreover, the obtained Ag films exhibited excellent stability during electrochemical CO_2 reduction as the Ag film was strongly bonded to the APTES layer. At a low

overpotential of 0.19 V, the N- and S-doped Ag film with an optimized N/S doping ratio of 1.75 achieved a CO FE of 75.7%. This value is higher than those previously reported for Ag-based electrocatalysts.

Declarations of competing interest

The authors declare no competing financial interest.

Appendix A. Supplementary data

Supplementary material related to this article can be found, in the online version, at doi:https://doi.org/10.1016/j.apcatb.2019.118045.

References

[1] J.S. Sawyer, Man-made carbon dioxide and the "Greenhouse" effect, Nature 239 (1972) 23, https://doi.org/10.1038/239023a0.
[2] S.J. Davis, K. Caldeira, H.D. Matthews, Future CO_2 emissions and climate change from existing energy infrastructure, Science 329 (2010) 1330, https://doi.org/10.1126/science.1188566.
[3] D.Y.C. Leung, G. Caramanna, M.M. Maroto-Valer, An overview of current status of carbon dioxide capture and storage technologies, Renew. Sustain. Energy Rev. 39 (2014) 426–443, https://doi.org/10.1016/j.rser.2014.07.093.
[4] R.M. Cuéllar-Franca, A. Azapagic, Carbon capture, storage and utilisation technologies: a critical analysis and comparison of their life cycle environmental impacts, J. CO2 Util 9 (2015) 82–102, https://doi.org/10.1016/j.jcou.2014.12.001.
[5] J. Qiao, Y. Liu, F. Hong, J. Zhang, A review of catalysts for the electroreduction of carbon dioxide to produce low-carbon fuels, Chem. Soc. Rev. 43 (2014) 631–675, https://doi.org/10.1039/C3CS60323G.
[6] D.D. Zhu, J.L. Liu, S.Z. Qiao, Recent advances in inorganic heterogeneous

electrocatalysts for reduction of carbon dioxide, Adv. Mater. 28 (2016) 3423–3452, https://doi.org/10.1002/adma.201504766.

[7] N.S. Spinner, J.A. Vega, W.E. Mustain, Recent progress in the electrochemical conversion and utilization of CO_2, Catal. Sci. Technol. 2 (2012) 19–28, https://doi.org/10.1039/C1CY00314C.

[8] K.P. Kuhl, T. Hatsukade, E.R. Cave, D.N. Abram, J. Kibsgaard, T.F. Jaramillo, Electrocatalytic conversion of carbon dioxide to methane and methanol on transition metal surfaces, J. Am. Chem. Soc. 136 (2014) 14107–14113, https://doi.org/10.1021/ja505791r.

[9] X. Lu, D.Y.C. Leung, H. Wang, M.K.H. Leung, J. Xuan, Electrochemical reduction of carbon dioxide to formic acid, ChemElectroChem 1 (2014) 836–849, https://doi.org/10.1002/celc.201300206.

[10] A.M. Appel, J.E. Bercaw, A.B. Bocarsly, H. Dobbek, D.L. DuBois, M. Dupuis, J.G. Ferry, E. Fujita, R. Hille, P.J.A. Kenis, C.A. Kerfeld, R.H. Morris, C.H.F. Peden, A.R. Portis, S.W. Ragsdale, T.B. Rauchfuss, J.N.H. Reek, L.C. Seefeldt, R.K. Thauer, G.L. Waldrop, Frontiers, opportunities, and challenges in biochemical and chemical catalysis of CO_2 fixation, Chem. Rev. 113 (2013) 6621–6658, https://doi.org/10.1021/cr300463y.

[11] Q. Lu, J. Rosen, Y. Zhou, G.S. Hutchings, Y.C. Kimmel, J.G. Chen, F. Jiao, A selective and efficient electrocatalyst for carbon dioxide reduction, Nat. Commun. 5 (2014) 3242, https://doi.org/10.1038/ncomms4242.

[12] W. Luc, C. Collins, S. Wang, H. Xin, K. He, Y. Kang, F. Jiao, Ag–Sn bimetallic catalyst with a core–shell structure for CO_2 reduction, J. Am. Chem. Soc. 139 (2017) 1885–1893, https://doi.org/10.1021/jacs.6b10435.

[13] T. Hatsukade, K.P. Kuhl, E.R. Cave, D.N. Abram, J.T. Feaster, A.L. Jongerius, C. Hahn, T.F. Jaramillo, Carbon dioxide electroreduction using a silver–zinc alloy, Energy Technol. 5 (2017) 955–961, https://doi.org/10.1002/ente.201700087.

[14] M.S. Jee, H.S. Jeon, C. Kim, H. Lee, J.H. Koh, J. Cho, B.K. Min, Y.J. Hwang, Enhancement in carbon dioxide activity and stability on nanostructured silver electrode and the role of oxygen, Appl. Catal. B: Environ. 180 (2016) 372–378, https://doi.org/10.1016/j.apcatb.2015.06.046.

[15] Y. Yoon, A.S. Hall, Y. Surendranath, Tuning of silver catalyst mesostructure promotes selective carbon dioxide conversion into fuels, Angew. Chem. 128 (2016) 15508–15512, https://doi.org/10.1002/anie.201607942.

[16] J. Rosen, G.S. Hutchings, Q. Lu, S. Rivera, Y. Zhou, D.G. Vlachos, F. Jiao, Mechanistic insights into the electrochemical reduction of CO_2 to CO on nanostructured Ag surfaces, ACS Catal. 5 (2015) 4293–4299, https://doi.org/10.1021/acscatal.5b00840.

[17] Z. Weng, J. Jiang, Y. Wu, Z. Wu, X. Guo, K.L. Materna, W. Liu, V.S. Batista, G.W. Brudvig, H. Wang, Electrochemical CO_2 reduction to hydrocarbons on a heterogeneous molecular Cu catalyst in aqueous solution, J. Am. Chem. Soc. 138 (2016) 8076–8079, https://doi.org/10.1021/jacs.6b04746.

[18] Y. Li, F. Cui, M.B. Ross, D. Kim, Y. Sun, P. Yang, Structure-sensitive CO_2 electroreduction to hydrocarbons on ultrathin 5-fold twinned copper nanowires, Nano Lett. 17 (2017) 1312–1317, https://doi.org/10.1021/acs.nanolett.6b05287.

[19] S. Gao, Y. Lin, X. Jiao, Y. Sun, Q. Luo, W. Zhang, D. Li, J. Yang, Y. Xie, Partially oxidized atomic cobalt layers for carbon dioxide electroreduction to liquid fuel, Nature 529 (2016) 68–71, https://doi.org/10.1038/nature16455.

[20] J. Chung, D.H. Won, J. Koh, E.-H. Kim, S.I. Woo, Hierarchical Cu pillar electrodes for electrochemical CO_2 reduction to formic acid with low overpotential, Phys. Chem. Chem. Phys. 18 (2016) 6252–6258, https://doi.org/10.1039/C5CP07964K.

[21] J.-M. Saveant, C. Tard, Attempts to catalyze the electrochemical CO_2-to-methanol conversion by biomimetic $2e– + 2H^+$ transferring molecules, J. Am. Chem. Soc. 138 (2016) 1017–1021, https://doi.org/10.1021/jacs.5b12138.

[22] M. Irfan Malik, Z.O. Malaibari, M. Atieh, B. Abussaud, Electrochemical reduction of CO_2 to methanol over MWCNTs impregnated with Cu_2O, Chem. Eng. Sci. 152 (2016) 468–477, https://doi.org/10.1016/j.ces.2016.06.035.

[23] W. Keim, Carbon monoxide: feedstock for chemicals, present and future, J. Organomet. Chem. 372 (1989) 15–23, https://doi.org/10.1016/0022-328X(89)87071-8.

[24] Y.-C. Hsieh, S.D. Senanayake, Y. Zhang, W. Xu, D.E. Polyansky, Effect of chloride anions on the synthesis and enhanced catalytic activity of silver nanocoral electrodes for CO_2 electroreduction, ACS Catal. 5 (2015) 5349–5356, https://doi.org/10.1021/acscatal.5b01235.

[25] Y.S. Ham, S. Choe, M.J. Kim, T. Lim, S.-K. Kim, J.J. Kim, Electrodeposited Ag catalysts for the electrochemical reduction of CO_2 to CO, Appl. Catal. B: Environ. 208 (2017) 35–43, https://doi.org/10.1016/j.apcatb.2017.02.040.

[26] C.-Y. Lee, Y. Zhao, C. Wang, D.R.G. Mitchell, G.G. Wallace, Rapid formation of self-organised Ag nanosheets with high efficiency and selectivity in CO_2 electroreduction to CO, Sustain. Energy Fuels 1 (2017) 1023–1027, https://doi.org/10.1039/C7SE00069C.

[27] H. Wang, Z. Han, L. Zhang, C. Cui, X. Zhu, X. Liu, J. Han, Q. Ge, Enhanced CO selectivity and stability for electrocatalytic reduction of CO_2 on electrodeposited nanostructured porous Ag electrode, J. CO2 Util. 15 (2016) 41–49, https://doi.org/10.1016/j.jcou.2016.04.013.

[28] S. Liu, H. Tao, L. Zeng, Q. Liu, Z. Xu, Q. Liu, J.-L. Luo, Shape-dependent electrocatalytic reduction of CO_2 to CO on triangular silver nanoplates, J. Am. Chem. Soc. 139 (2017) 2160–2163, https://doi.org/10.1021/jacs.6b12103.

[29] M.R. Singh, Y. Kwon, Y. Lum, J.W. Ager, A.T. Bell, Hydrolysis of electrolyte cations

enhances the electrochemical reduction of CO_2 over Ag and Cu, J. Am. Chem. Soc. 138 (2016) 13006–13012, https://doi.org/10.1021/jacs.6b07612.

[30] J. Choi, M.J. Kim, S.H. Ahn, I. Choi, J.H. Jang, Y.S. Ham, J.J. Kim, S.-K. Kim, Electrochemical CO_2 reduction to CO on dendritic Ag–Cu electrocatalysts prepared by electrodeposition, Chem. Eng. J. 299 (2016) 37–44, https://doi.org/10.1016/j.cej.2016.04.037.

[31] Z. Chang, S. Huo, W. Zhang, J. Fang, H. Wang, The tunable and highly selective reduction products on Ag@Cu bimetallic catalysts toward CO_2 electrochemical reduction reaction, J. Phys. Chem. C 121 (2017) 11368–11379, https://doi.org/10.1021/acs.jpcc.7b01586.

[32] M. Ma, B.J. Trześniewski, J. Xie, W.A. Smith, Selective and efficient reduction of carbon dioxide to carbon monoxide on oxide-derived nanostructured silver electrocatalysts, Angew. Chem. Int. Edit. 55 (2016) 9748–9752.

[33] H.-K. Lim, H. Shin, W.A. Goddard, Y.J. Hwang, B.K. Min, H. Kim, Embedding covalency into metal catalysts for efficient electrochemical conversion of CO_2, J. Am. Chem. Soc. 136 (2014) 11355–11361, https://doi.org/10.1002/anie.201604654.

[34] C. Kim, H.S. Jeon, T. Eom, M.S. Jee, H. Kim, C.M. Friend, B.K. Min, Y.J. Hwang, Achieving selective and efficient electrocatalytic activity for CO_2 reduction using immobilized silver nanoparticles, J. Am. Chem. Soc. 137 (2015) 13844–13850, https://doi.org/10.1021/jacs.5b06568.

[35] C. Kim, T. Eom, M.S. Jee, H. Jung, H. Kim, B.K. Min, Y.J. Hwang, Insight into electrochemical CO_2 reduction on surface-molecule-mediated Ag nanoparticles, ACS Catal. 7 (2017) 779–785, https://doi.org/10.1021/acscatal.6b01862.

[36] X. Peng, S.G. Karakalos, W.E. Mustain, Preferentially oriented Ag nanocrystals with extremely high activity and faradaic efficiency for CO_2 electrochemical reduction to CO, ACS Appl. Mater. Interfaces 10 (2018) 1734–1742, https://doi.org/10.1021/acsami.7b16164.

[37] Z. He, T. Liu, J. Tang, C. Zhou, L. Wen, J. Chen, S. Song, Highly active, selective and stable electroreduction of carbon dioxide to carbon monoxide on a silver catalyst with truncated hexagonal bipyramidal shape, Electrochim. Acta 222 (2016) 1234–1242, https://doi.org/10.1016/j.electacta.2016.11.097.

[38] K. Sun, L. Wu, W. Qin, J. Zhou, Y. Hu, Z. Jiang, B. Shen, Z. Wang, Enhanced electrochemical reduction of CO_2 to CO on Ag electrocatalysts with increased unoccupied density of states, J. Mater. Chem. A 4 (2016) 12616–12623, https://doi.org/10.1016/10.1039/C6TA04325A.

[39] R. Daiyan, X. Lu, H. Ng, R. Amal, Highly selective conversion of CO_2 to CO achieved by a three-dimensional porous silver electrocatalyst, ChemistrySelect 2 (2017) 879–884, https://doi.org/10.1002/slct.201601980.

[40] A.F. Scarpettini, A.V. Bragas, Coverage and aggregation of gold nanoparticles on silanized glasses, Langmuir 26 (2010) 15948–15953, https://doi.org/10.1021/la102937b.

[41] Y.U. Ko, S.-r. Cho, K.S. Choi, Y. Park, S.T. Kim, N.H. Kim, S.Y. Kim, S.T. Chang, Microlitre scale solution processing for controlled, rapid fabrication of chemically derived graphene thin films, J. Mater. Chem. 22 (2012) 3606–3613, https://doi.org/10.1039/C2JM15299A.

[42] T. Okamoto, I. Yamaguchi, T. Kobayashi, Local plasmon sensor with gold colloid monolayers deposited upon glass substrates, Opt. Lett. 25 (2000) 372–374, https://doi.org/10.1364/OL.25.000372.

[43] X. Su, S.F.Y. Li, S.J. O'Shea, Au nanoparticle- and silver-enhancement reaction-amplified microgravimetric biosensor, Chem. Commun. (2001) 755–756, https://doi.org/10.1039/B009768N.

[44] R.-Q. Liang, C.-Y. Tan, K.-C. Ruan, Colorimetric detection of protein microarrays based on nanogold probe coupled with silver enhancement, J. Immunol. Methods 285 (2004) 157–163, https://doi.org/10.1016/j.jim.2003.11.008.

[45] W. Ahliah Ismail, Z.A. Ali, R. Puteh, Transparent nanocrystallite silver for antibacterial coating, J. Nanomater. 2013 (2013) 901452, , https://doi.org/10.1155/2013/901452.

[46] J.J. Jing, J. Xie, G.Y. Chen, W.H. Li, M.M. Zhang, Preparation of nickel–silver core–shell nanoparticles by liquid-phase eduction for use in conductive paste, J. Exp. Nanosci. 10 (2015) 1347–1356, https://doi.org/10.1080/17458080.2015.1012751.

[47] S. Xu, X. Ji, W. Xu, X. Li, L. Wang, Y. Bai, B. Zhao, Y. Ozaki, Immunoassay using probe-labelling immunogold nanoparticles with silver staining enhancement via surface-enhanced Raman scattering, Analyst 129 (2004) 63–68, https://doi.org/10.1039/b313094k.

[48] I. Romero, J. Aizpurua, G.W. Bryant, F.J.Gd. Abajo, Plasmons in nearly touching metallic nanoparticles: singular response in the limit of touching dimers, Opt. Express 14 (2006) 9988–9999, https://doi.org/10.1364/OE.14.009988.

[49] S. Jeong, H.C. Song, W.W. Lee, Y. Choi, S.S. Lee, B.-H. Ryu, Combined role of well-dispersed aqueous Ag ink and the molecular adhesive layer in inkjet printing the narrow and highly conductive Ag features on a glass substrate, J. Phys. Chem. C 114 (2010) 22277–22283, https://doi.org/10.1021/jp106994t.

[50] B. Khezri, A.C. Fisher, M. Pumera, CO_2 reduction: the quest for electrocatalytic materials, J. Mater. Chem. A 5 (2017) 8230–8246, https://doi.org/10.1039/C6TA09875D.

[51] H. Park, J. Choi, H. Kim, E. Hwang, D.-H. Ha, S.H. Ahn, S.-K. Kim, AgIn dendrite catalysts for electrochemical reduction of CO_2 to CO, Appl. Catal. B: Environ. 219 (2017) 123–131, https://doi.org/10.1016/j.apcatb.2017.07.038.